Production and transport of vorticity in two-dimensional Rayleigh–Bénard convection cell

Ao Xu (徐翱), Ben-Rui Xu (许本瑞), Li-Sheng Jiang (姜丽升), et al.

View Online Export Citation CrossMark

Production and transport of vorticity in two-dimensional Rayleigh–Bénard convection cell

Ao Xu (徐翱),[1,2] [iD] Ben-Rui Xu (许本瑞),[1] Li-Sheng Jiang (姜丽升),[1] and Heng-Dong Xi (郗恒东)[1,2,a] [iD]

AFFILIATIONS

[1]School of Aeronautics, Northwestern Polytechnical University, Xi'an 710072, China
[2]Institute of Extreme Mechanics, Northwestern Polytechnical University, Xi'an 710072, China

[a]Author to whom correspondence should be addressed: hengdongxi@nwpu.edu.cn

ABSTRACT

We present a numerical study of vorticity production and transport in the two-dimensional Rayleigh–Bénard (RB) convection. Direct numerical simulations are carried out in the Rayleigh number (Ra) range $10^5 \leq Ra \leq 10^6$, the Prandtl number (Pr) of 0.71, and the aspect ratio (Γ) of the convection cell range $0.75 \leq \Gamma \leq 6$. We found that the flow structure and temperature distribution vary with Γ greatly due to multiple vortices interaction. Further investigation on the vorticity production and transport reveals that, in the RB convection, in addition to the vorticity production due to wall shear stress, buoyancy produces significant vorticity in the bulk region. The produced vorticity is transported via advection and diffusion. An interesting finding is that the main vortices and the corner vortices can be visualized via the contour of buoyancy-produced vorticity. Although a vigorous definition of the vortex is still lacking in the community, our efficient vortex visualization approach in the RB convection may shed light on further research toward vortex identification. We also found that the spatial distribution of vorticity flux along the wall is positively correlated with that of the Nusselt number (Nu), suggesting the amount of vorticity that enters the flow is directly related to the amount of thermal energy that enters the flow.

Published under an exclusive license by AIP Publishing. https://doi.org/10.1063/5.0072873

I. INTRODUCTION

Thermal convection occurs ubiquitously in nature and has wide applications in industry, such as convection over the city,[1] convection in the indoor environment,[2,3] convection in the heat exchanger reactor,[4] and so on. A canonic flow system for studying thermal convection is Rayleigh–Bénard (RB) convection,[5,6] in which the fluid is heated from the bottom wall and cooled from the top wall. In thermal convection cells, approaches to enhance heat transfer efficiency include creating roughness on the heating walls,[7,8] geometrical confinement of the convection cell,[9,10] vibration-induced boundary-layer destabilization,[11,12] and many others.

Previous studies have revealed the connections between heat transfer efficiency (in terms of dimensionless Nusselt number, Nu) and flow structures.[13–20] For example, Sun _et al._[13] measured the Nu in both leveled and tilted cylindrical cells, in which the large-scale circulation is either azimuthal or locked in a particular orientation, respectively. They found that the Nu is larger in the leveled cell than that in the tilted one, thus demonstrating that different flow structures can give rise to different values of Nu. Xi _et al._[14] further observed that both

the single-roll and the double-roll flow structures exist in the large-scale flow. They examined the averaged Nu corresponding to a particular flow structure, and they found that the single-roll flow structure is more efficient for heat transfer than the double-roll structure. Later, Xi _et al._[15] found that Nu has a momentary overshoot above its average value during flow reversal event, which is also numerically verified by Xu _et al._[16] The overshoot in Nu was attributed to more coherent flow or plumes for the short period of time during reversal. van der Poel _et al._[17,18] simulated the aspect ratio dependence of heat transfer efficiency in a two-dimensional (2D) square cell. They conditionally averaged Nu based on flow structures, and they found that heat transfer is more efficient with less vertically arranged vortex or less horizontally elongated vortex. Xu _et al._[16] adopted the Fourier mode decomposition and the proper orthogonal decomposition to extract the coherent flow structure. They showed that the single-roll mode, the horizontally stacked double-roll mode, and the quadrupolar flow mode are more efficient for heat transfer on average; in contrast, the vertically stacked double-roll mode is inefficient for heat transfer on average.[16]

On the other hand, it is advantageous to interpret the fluid flows in terms of vorticity, which is defined as the curl of velocity $\omega = \nabla \times \mathbf{u}$.[21,22] The vorticity represents the rotation of a fluid particle, and only the shear stresses can rotate the fluid particle. As for the pressure and the normal viscous stresses, they act through the center of the fluid particle and cannot rotate fluid particles. Thus, analyzing vorticity dynamics will reveal physical mechanisms for fluid flows and associate transport processes (e.g., heat transfer, mass transfer, ion transfer) that may be hidden from the velocity and pressure fields. In the industry, various vortex generators have been designed to enhance transfer in heat exchanger reactors;[23,24] however, most of those studies focused on a global relationship between the velocity field and heat transfer efficiency, and the role of vorticity transport in heat transfer enhancement remains unclear.

In this work, we will provide a comprehensive analysis of vorticity production and transport in the simple yet canonic RB convection. Our motivation is to reveal the connections between heat transfer efficiency and the vorticity field. The rest of the paper is organized as follows. In Sec. II, we will present the numerical method for simulating incompressible thermal convection. The in-house numerical solver based on the lattice Boltzmann (LB) method will be introduced. In Sec. III, we will first provide general flow and heat transfer features in the convection cells; after that, we will analyze vorticity production due to wall shear stress and buoyancy, as well as vorticity transport due to advection and diffusion. In Sec. IV, the main findings of the present work are summarized.

II. NUMERICAL METHOD
A. Mathematical model for thermal convection

We consider incompressible thermal flows under the Boussinesq approximation. The temperature is treated as an active scalar, and its influence on the velocity field is realized through the buoyancy term. The viscous heat dissipation and compression work are neglected, and all the transport coefficients are assumed to be constants. Then, the governing equations can be written as

$$\nabla \cdot \mathbf{u} = 0, \tag{1a}$$

$$\frac{\partial \mathbf{u}}{\partial t} + \mathbf{u} \cdot \nabla \mathbf{u} = -\frac{1}{\rho_0} \nabla P + \nu \nabla^2 \mathbf{u} + g \beta_T (T - T_0) \hat{\mathbf{y}}, \tag{1b}$$

$$\frac{\partial T}{\partial t} + \mathbf{u} \cdot \nabla T = \alpha_T \nabla^2 T, \tag{1c}$$

where $\mathbf{u} = (u, v)$, P, and T are velocity, pressure, and temperature of the fluid, respectively. P_0, ρ_0, and T_0 are the reference pressure, density, and temperature, respectively. β_T, ν, and α_T are the thermal expansion coefficient, kinematic viscosity, and thermal diffusivity, respectively. g is the gravity acceleration value. $\hat{\mathbf{y}}$ is the unit vector parallel to the gravity. With the following non-dimensional group

$$\mathbf{x}^* = \mathbf{x}/H, \quad t^* = t/\sqrt{H/(g\beta_T \Delta_T)}, \quad \mathbf{u}^* = \mathbf{u}/\sqrt{g\beta_T \Delta_T H},$$
$$P^* = (P - P_0)/(\rho_0 g \beta_T \Delta_T H), \quad T^* = (T - T_0)/\Delta_T. \tag{2}$$

Then, Eq. (1) can be rewritten in dimensionless form as

$$\nabla \cdot \mathbf{u}^* = 0, \tag{3a}$$

$$\frac{\partial \mathbf{u}^*}{\partial t^*} + \mathbf{u}^* \cdot \nabla \mathbf{u}^* = -\nabla P^* + \sqrt{\frac{Pr}{Ra}} \nabla^2 \mathbf{u}^* + T^* \hat{\mathbf{y}}, \tag{3b}$$

$$\frac{\partial T^*}{\partial t^*} + \mathbf{u}^* \cdot \nabla T^* = \sqrt{\frac{1}{PrRa}} \nabla^2 T^*. \tag{3c}$$

Here, H is the cell height and Δ_T is the temperature difference between heating and cooling walls. P_0 is the reference pressure. In this paper, unless otherwise stated, the dimensionless variable is denoted with a superscript star. The two dimensionless parameters are the Rayleigh number (Ra) and the Prandtl number (Pr), which are defined as

$$Ra = \frac{g\beta_T \Delta_T H^3}{\nu \alpha_T}, \quad Pr = \frac{\nu}{\alpha_T}. \tag{4}$$

B. The lattice Boltzmann method for incompressible thermal flows

The LB method to solve fluid flows and heat transfer is based on the double distribution function approach. The advantages of the LB method include easy implementation and parallelization as well as low numerical dissipation.[25–27] Specifically, we chose a D2Q9 model for the Navier–Stokes equations to simulate fluid flows and a D2Q5 model for the energy equation to simulate heat transfer. To enhance the numerical stability, the multi-relaxation-time collision operator is adopted in the evolution equations of both density and temperature distribution functions. The evolution equation of the density distribution function is written as

$$f_i(\mathbf{x} + \mathbf{e}_i \delta_t, t + \delta_t) - f_i(\mathbf{x}, t)$$
$$= -(\mathbf{M}^{-1}\mathbf{S})_{ij}\left[\mathbf{m}_j(\mathbf{x}, t) - \mathbf{m}_j^{(eq)}(\mathbf{x}, t)\right] + \delta_t F_i', \tag{5}$$

where f_i is the density distribution function, $\mathbf{x}$ is the fluid parcel position, t is the time, and δ_t is the time step. $\mathbf{e}_i$ is the discrete velocity along the ith direction. $\mathbf{M}$ is a 9×9 orthogonal transformation matrix that projects the density distribution function f_i and its equilibrium $f_i^{(eq)}$ from the velocity space onto the moment space, such that $\mathbf{m} = \mathbf{M}\mathbf{f}$ and $\mathbf{m}^{(eq)} = \mathbf{M}\mathbf{f}^{(eq)}$. $\mathbf{S}$ is the diagonal relaxation matrix. The macroscopic density ρ and velocity $\mathbf{u}$ are obtained from the density distribution function as

$$\rho = \sum_{i=0}^{8} f_i, \quad \mathbf{u} = \frac{1}{\rho}\left(\sum_{i=0}^{8} \mathbf{e}_i f_i + \mathbf{F}/2\right). \tag{6}$$

The evolution equation of temperature distribution function is written as

$$g_i(\mathbf{x} + \mathbf{e}_i \delta_t, t + \delta_t) - g_i(\mathbf{x}, t) = -(\mathbf{N}^{-1}\mathbf{Q})_{ij}\left[\mathbf{n}_j(\mathbf{x}, t) - \mathbf{n}_j^{(eq)}(\mathbf{x}, t)\right], \tag{7}$$

where g_i is the temperature distribution function. $\mathbf{N}$ is a 5×5 orthogonal transformation matrix that projects the temperature distribution function g_i and its equilibrium $g_i^{(eq)}$ from the velocity space onto the moment space, such that $\mathbf{n} = \mathbf{N}\mathbf{g}$ and $\mathbf{n}^{(eq)} = \mathbf{N}\mathbf{g}^{(eq)}$. $\mathbf{Q}$ is the diagonal relaxation matrix. The macroscopic temperature T is obtained from the temperature distribution function as

$$T = \sum_{i=0}^{4} g_i. \tag{8}$$

Our in-house LB solver is accelerated with OpenACC directives to utilize the computing power of GPUs.[28] More numerical details of the LB

method and validation of the in-house solver can be found in our previous work.[29–31]

C. Simulation settings

The top and bottom walls of the convection cell are kept at constant cold and hot temperature, respectively, while the other two vertical walls are adiabatic. All four walls impose no-slip velocity boundary conditions. The dimension of the cell is $L \times H$. Here, L is the cell length. Simulation results are provided for the Ra in the range $10^5 \leq Ra \leq 10^6$, the Pr of 0.71, and cell aspect ratio ($\Gamma = L/H$) in the range $0.75 \leq \Gamma \leq 6$. The criterion for reaching a steady state is

$$\frac{\sum_i \| \mathbf{u}(x_i, t + 2000\delta_t) - \mathbf{u}(x_i, t) \|_2}{\sum_i \| \mathbf{u}(x_i, t) \|_2} < 10^{-9},$$

$$\frac{\sum_i |T(x_i, t + 2000\delta_t) - T(x_i, t)|_2}{\sum_i |T(x_i, t)|_2} < 10^{-9}. \quad (9)$$

For unsteady flows, after the flows reach the statistically stationary state, we take average time of t_{avg} to obtain statistically convergent results. The time-averaged value of variable ϕ is define as $\bar{\phi} = \int_{t_1}^{t_2} \phi \, dt / (t_2 - t_1)$, where $t_2 - t_1 = t_{avg}$ is the time duration of the flow in the fully developed state.

We first refine the grid to check the convergence behaviors of the in-house LB solvers. We calculated response parameters including the Nusselt number (Nu) and the Reynolds number (Re), which describe the heat transfer efficiency and flow strength, respectively,
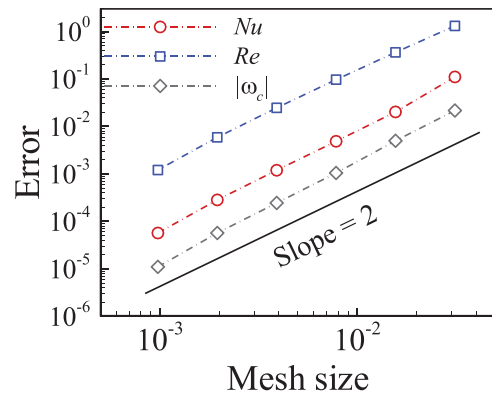
$$Nu = \sqrt{Ra \cdot Pr} \langle v^* T^* \rangle_{V,t} + 1, \quad Re = \frac{\sqrt{\langle (u^2 + v^2) \rangle_{V,t}} H}{\nu}. \quad (10)$$

Here, $\langle \cdot \rangle_{V,t}$ denotes the spatial and temporal average. In Table I, we list the steady solution of Nu, Re, and the absolute value of vorticity at cell center ($|\omega_c|$) obtained at $Ra = 10^6$, $Pr = 0.71$, and $\Gamma = 1$. From Table I, we can see that results calculated from the LB solver monotonous converge.

To quantitatively evaluate the spatial convergence order, we assume the results obtained at the largest grid of 2048^2 are accurate

TABLE I. Spatial convergence of the in-house lattice Boltzmann (LB) solver. The columns include grid number, the Nusselt number (Nu), the Reynolds number (Re), and the absolute value of vorticity at cell center ($|\omega_c|$) for $Ra = 10^6$, $Pr = 0.71$, and $\Gamma = 1$.

Grid	Nu	Re	$|\omega_c|$
32^2	6.4393	274.40	1.5280
64^2	6.3489	275.36	1.5114
128^2	6.3336	275.62	1.5074
256^2	6.3299	275.70	1.5066
512^2	6.3290	275.72	1.5064
1024^2	6.3287	275.72	1.5064
2048^2	6.3287	275.72	1.5064

FIG. 1. Spatial convergence of the in-house LB solver. The solid line is to guide the eye.

and calculate the error as $\text{Error}(\delta x) = |\mathscr{F}(\delta x) - \mathscr{F}(1/2048)|$. Here, $\mathscr{F}(\delta x)$ denotes flow variables calculated with a mesh size of δx. From Fig. 1, we can see that the LB solver is second-order spatial accuracy for simulating velocity and temperature fields. In addition, the vorticity field, which is obtained from the curl of velocity field data using a third-order finite difference scheme, also exhibits second-order spatial accuracy. It should be noted that numerics in Table I are presented with five significant numbers for clarity of writing, while the data in Fig. 1 are calculated with eight significant numbers. The mesh independent tests indicate that a grid resolution of 256 is adequate for the simulation. Thus, we use at least 256 grids to resolve the cell length or the cell height. Other detailed simulation parameters are listed in Table II. In addition, we list the response parameters of Nu and Re in Table II. At fixed Ra and Pr, with the increase in Γ, both the Nu and Re gradually increase to an asymptotic value.

TABLE II. Parameters of the different simulations (columns from left to right): Rayleigh number Ra, Prandlt number Pr, aspect ratio Γ, grid number, flow state (either steady state or unsteady state), average time t_{avg} of the simulation in free fall time unit $t_f = \sqrt{H/(g\beta_T \Delta_T)}$ for unsteady flows, Nusselt number Nu, and Reynolds number Re.

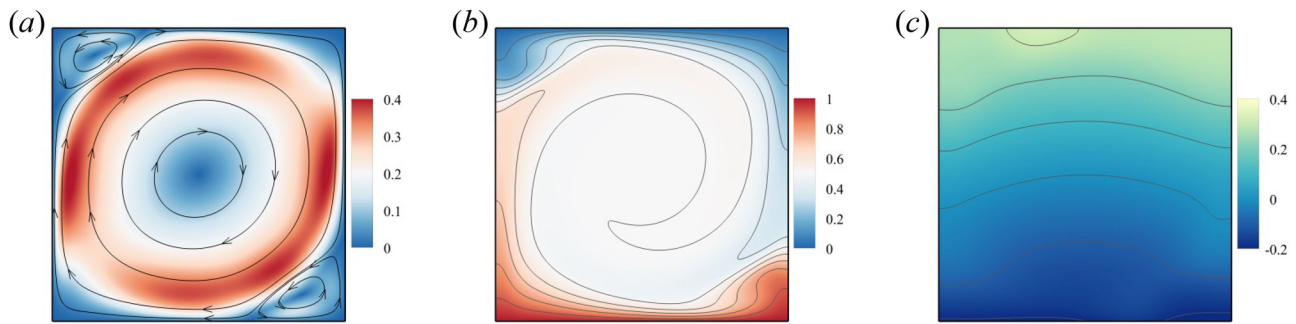| Ra	Pr	Γ	Grid	Flow state	t_{avg}	Nu	Re
1×10^5	0.71	0.75	256×342	Unsteady	$1000 \, t_f$	2.44	49.47
1×10^5	0.71	1	256×256	Steady	$\cdots$	3.92	84.43
1×10^5	0.71	2	512×256	Steady	$\cdots$	4.43	100.97
1×10^5	0.71	4	1024×256	Steady	$\cdots$	4.75	109.29
1×10^5	0.71	6	1536×256	Steady	$\cdots$	4.84	111.58
3×10^5	0.71	0.75	256×342	Steady	$\cdots$	3.34	99.93
3×10^5	0.71	1	256×256	Steady	$\cdots$	5.03	151.57
3×10^5	0.71	2	512×256	Steady	$\cdots$	5.73	182.68
3×10^5	0.71	4	1024×256	Steady	$\cdots$	6.22	199.36
3×10^5	0.71	6	1536×256	Steady	$\cdots$	6.37	203.89
1×10^6	0.71	0.75	256×342	Steady	$\cdots$	4.62	202.33
1×10^6	0.71	1	256×256	Steady	$\cdots$	6.33	275.70
1×10^6	0.71	2	512×256	Steady	$\cdots$	7.39	340.87
1×10^6	0.71	4	1024×256	Steady	$\cdots$	8.25	377.48
1×10^6	0.71	6	1536×256	Unsteady	$1000 \, t_f$	8.47	386.54

FIG. 2. (a) Contour of velocity magnitude (superposed with streamlines) $\sqrt{u^{*2}+v^{*2}}$, (b) contour of temperature T^*, and (c) contour of pressure P^* at $Ra = 10^6$, $Pr = 0.71$, and $\Gamma = 1$.

III. RESULTS AND DISCUSSION

A. General flow and heat transfer features

We first present general flow and heat transfer patterns in the convection cell. Figure 2 shows the contour of velocity magnitude, temperature field, and pressure field in the RB convection at $Ra = 10^6$, $Pr = 0.71$, and $\Gamma = 1$. Here, the reference temperature is chosen as the temperature of the cold wall, that is, $T_0 = T_{cold}$ such that the dimensionless temperature varies between zero and one. The reference pressure is chosen as the pressure at the cell center, that is, $P_0 = P(x^* = 0.5, y^* = 0.5)$ such that the dimensionless pressure at the cell center equals zero. In the RB convection, velocity magnitude exhibits large values near all four walls. In the bulk region of the RB convection, the clockwise rotated large-scale vortex exhibits a circular shape; near the top-left and bottom-right corners, there exist two counterclockwise rotated small vortices [see Fig. 2(a)]. Thin thermal boundary layers appear near the bottom and top horizontal walls [see Fig. 2(b)], where the fluids are heating and cooling, respectively. Driven by the clockwise large-scale circulation, detached hot plumes arise along the left adiabatic wall, and cold plumes fall along the right adiabatic wall. From the pressure field [see Fig. 2(c)], we observe a strong gradient of pressure along the vertical direction, while the pressure contour is slightly twisted along the horizontal direction. It should be noted that the pressure P shown here (and the corresponding dimensionless one) is based on the Boussinesq approximation, and it is related to the hydrodynamic pressure p_{N-S} via the relation of $P = p_{N-S} + \rho_0 g y$. For the dimensionless pressure under the Boussinesq approximation $P^* = (P - P_0)/(\rho_0 g \beta_T \Delta_T H)$, we can rewrite it as $P^* = [p_{N-S} - (p_{N-S})_0]/(\rho_0 g \beta_T \Delta_T H) + (y^* - 0.5)/(\beta_T \Delta_T)$, which indicates there is an additional term $(y^* - 0.5)/(\beta_T \Delta_T)$ compared to that in the dimensionless hydrodynamic pressure $p_{N-S}^* = [p_{N-S} - (p_{N-S})_0]/(\rho_0 g \beta_T \Delta_T H)$.

In the above, we discussed flow and heat transfer patterns in the convection cell of a unit square, that is, cell aspect ratio $\Gamma = 1$. Next, we focus on rectangular cells with $\Gamma > 1$ and $\Gamma < 1$, respectively. In Fig. 3, we show flow and heat transfer patterns in the RB convection with $\Gamma = 2$. We can observe two horizontally stacked main vortices in the $\Gamma = 2$ cell [see Fig. 3(a)]. These two counter-rotating vortices carry hot rising plumes along the vertical left and right walls. At the top wall, the fluids are cooling down, cold plumes emerge and they fall along the vertical mid-plane of the cell, and the temperature field preserves left-right symmetry, as shown in

Fig. 3(b). The contour of the pressure field in the RB convection [see Fig. 3(c)] is also twisted along the horizontal direction, and the trend is more obvious where the falling cold plumes eject on the hot bottom walls.
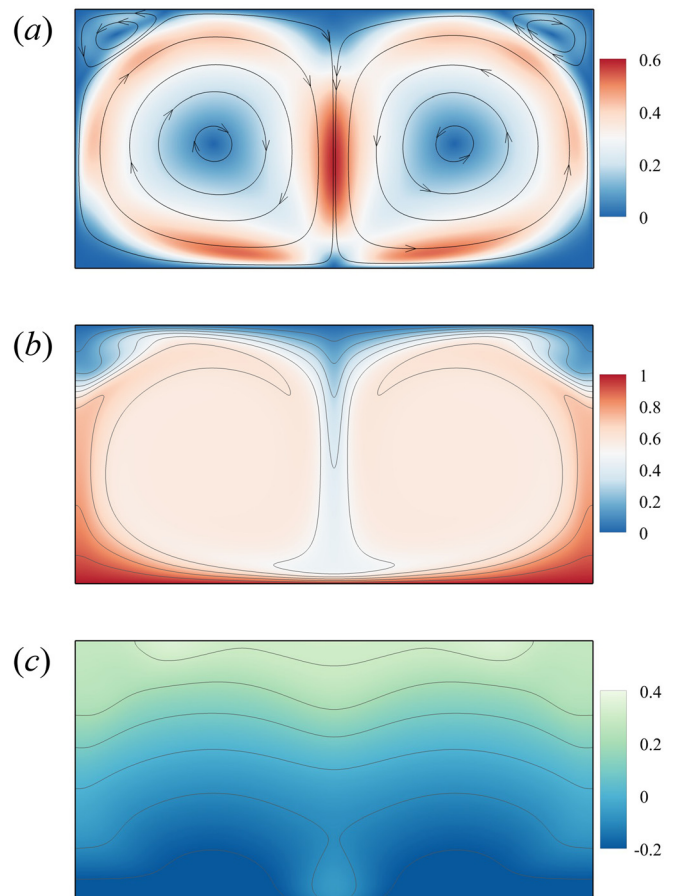

FIG. 3. (a) Contour of velocity magnitude (superposed with streamlines) $\sqrt{u^{*2}+v^{*2}}$, (b) contour of temperature T^*, (c) contour of pressure P^* at $Ra = 10^6$, $Pr = 0.71$, and $\Gamma = 2$.

Figure 4 further presents flow and heat transfer patterns in the RB convection with $\Gamma = 0.75$. We observe two vertically stacked main vortices in the $\Gamma = 0.75$ cell [see Fig. 4(a)]. The velocity magnitude reaches its maximum at the horizontal mid-plane, where the two main vortices interact. The bottom counterclockwise rotated vortex carries hot rising plumes, while the top clockwise rotated vortex carries cold falling plumes [see Fig. 4(b)]. The plumes exchange thermal energy at the horizontal mid-plane, and the temperature field preserves the top-bottom symmetry. In addition, the contour of the pressure field along the horizontal direction in the $\Gamma = 0.75$ cell [see Fig. 4(c)] is less twisted than that in the $\Gamma = 2$ cell [see Fig. 3(c)].

B. Vorticity production due to wall shear stress

To describe how much vorticity is entering the flow from the wall, we used the metrics of vorticity flux $\sigma_i = -\nu n_j \partial_j \omega_i$. Here, n_i is the plane orientation. In two dimensions, we only have non-zero components of vorticity as $\omega_z = \partial v / \partial x - \partial u / \partial y$. Thus, the vorticity flux along the vertical walls (i.e., $n_y = 0$) is $\sigma_z = -\nu n_x \partial_x \omega_z$, and the vorticity flux along the horizontal walls (i.e., $n_x = 0$) is $\sigma_z = -\nu n_y \partial_y \omega_z$. On the other hand, the heat flux perpendicular to the wall is $q_i = -\kappa \partial_i T$, and we normalize the heat flux with that due to pure conduction $\kappa \Delta_T H$, and then, we can use the dimensionless Nusselt number at the wall $Nu = q_i / (\kappa \Delta_T / H) = -\partial_{i^*} T^*$ to describe how much thermal energy is entering the flow. Here, κ denotes the thermal conductivity of the fluid. In Fig. 5, we plot the distribution of dimensionless vorticity flux $\sigma_i^* = -\sqrt{Pr/Ra} \cdot n_{j^*} \partial_{j^*} \omega_i^*$ and the normalized Nusselt number Nu/Nu_0 along top and bottom walls. Here, Nu_0 denotes the maximum value of Nu along all four walls. In the $\Gamma = 1$ cell [see Figs. 5(a) and 5(b)], the spatial distribution of the σ_i^* profile and the Nu profile is antisymmetric along the top and bottom walls. Along the horizontal walls, we can observe one peak and one valley near the central part of the wall. Here, the negative values of σ_i^* imply the vorticity that enters the flow is clockwise rotating. Both the positive and negative neighboring vorticity lead to enhanced thermal energy that enters the flow, and thus, we can observe a peak in the Nu.

In the $\Gamma = 2$ cell [see Figs. 5(c) and 5(d)], along the top (or the bottom) wall, the minimum values of Nu correspond to the positions where cold (or hot) plumes are released, and the maximum values of Nu correspond to the positions where hot (or cold) plumes are imping and penetrating the wall. Previously, Kenjereš and Hanjalić[32] reported the asymmetric of the Nu profile along the top and bottom walls in the $\Gamma > 1$ cell. Here, we found that the σ_i^* profile along the top and bottom walls is also asymmetric. More importantly, we found the spatial distribution of Nu along the heating and cooling walls can be well explained by the spatial distribution of σ_i^*. In the σ_i^* profile, a peak and a valley imply vorticity with opposite rotating direction is entering the flow; correspondingly, we can then observe a peak in the Nu profile. The reason is that the amount of vorticity (regardless of the rotating direction) that enters the flow is directly related to the amount of thermal energy that enters the flow. In Fig. 5(c), along the top wall, there are two pairs of peak and valley in the vorticity flux profile, and thus, there are two peaks in the Nu profile. In Fig. 5(d), along the bottom wall, there is one peak and one valley in the vorticity flux profile, and thus, there is only one peak in the Nu profile. In the $\Gamma = 0.75$ cell [see Figs. 5(e) and 5(f)], the two large-scale vortices are vertically stacked, and there is only one peak and valley in the σ_i^* profile along the horizontal walls, which is similar to that in the $\Gamma = 1$ cell. Correspondingly, the Nu profile shows a peak where extreme values of σ_i^* appear. Thus, we can analyze the spatial distribution of Nu along the heating and cooling walls via the vorticity flux along the wall.

Although vorticity can be viewed as the signatures of fluid motion, it is the pressure gradients that drive the flow. In the vorticity transport equation, the pressure does not appear; thus, it does not directly change the vorticity. It should be noted that the buoyancy appears in the momentum equation as an external body force, and thus, the effective pressure gradients are a combination of original pressure gradients and buoyancy. In Fig. 6, we show the dimensionless effective pressure gradients (i.e., ∇P_x^* and $\nabla P_y^* - T^*$) in the RB convection. We are particularly interested in the pressure gradients along the wall, which is necessary to sustain a flux of vorticity into the fluid. Because the velocity is zero at the wall, from the momentum equation, we have $\nabla P^* - T^* \hat{\mathbf{y}} = -\sqrt{Pr/Ra} \nabla \times \boldsymbol{\omega}^*$. Comparing Fig. 5 with Fig. 6, we can verify that positive σ_i^* along the bottom (or top) wall is indeed caused by the positive (or negative) value of horizontal effective pressure gradient.
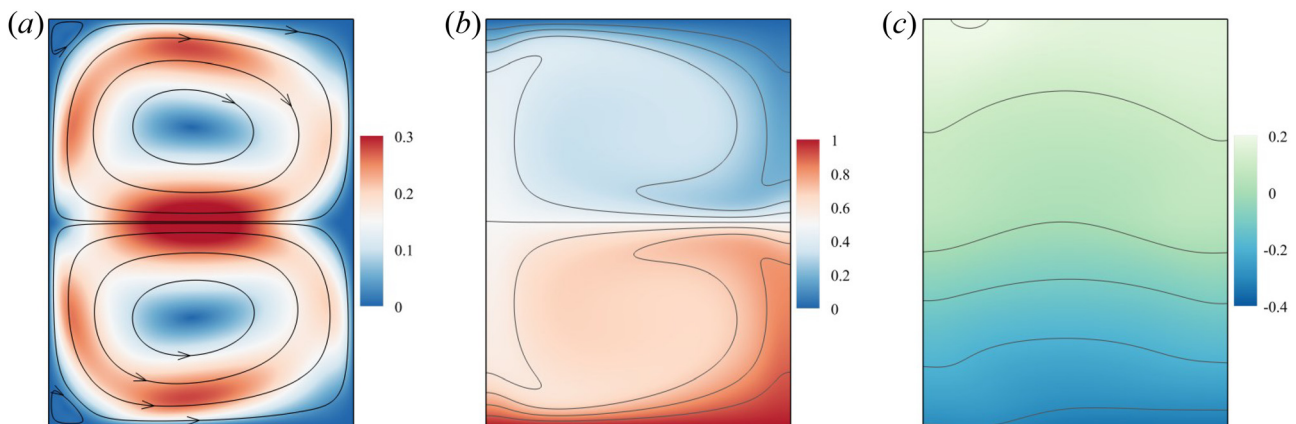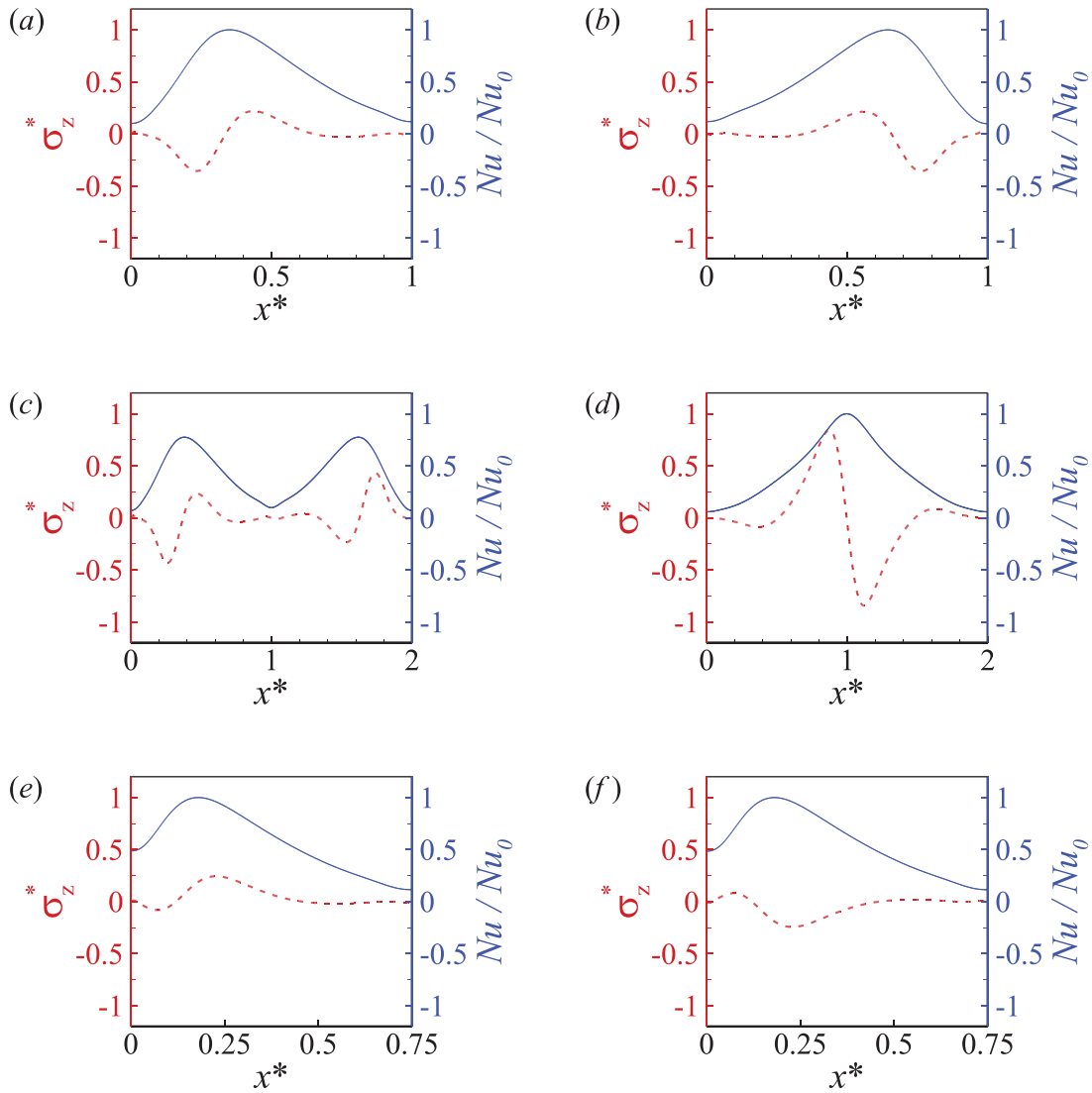

FIG. 4. (a) Contour of velocity magnitude (superposed with streamlines) $\sqrt{u^{*2} + v^{*2}}$, (b) contour of temperature T^*, (c) contour of pressure P^* at $Ra = 10^6$, $Pr = 0.71$, and $\Gamma = 0.75$.

FIG. 5. Distribution of dimensionless vorticity flux $\sigma_i^* = -\sqrt{Pr/Ra} \cdot n_{j} \cdot \partial_{j} \cdot \omega_i^*$ (red dash-dot line) and normalized Nusselt number Nu/Nu_0 (blue solid line) along the top cooling wall (left-column) and bottom heating wall (right-column) at $Ra = 10^6$, $Pr = 0.71$, (a) and (b) $\Gamma = 1$, (c) and (d) $\Gamma = 2$, (e) and (f) $\Gamma = 0.75$.
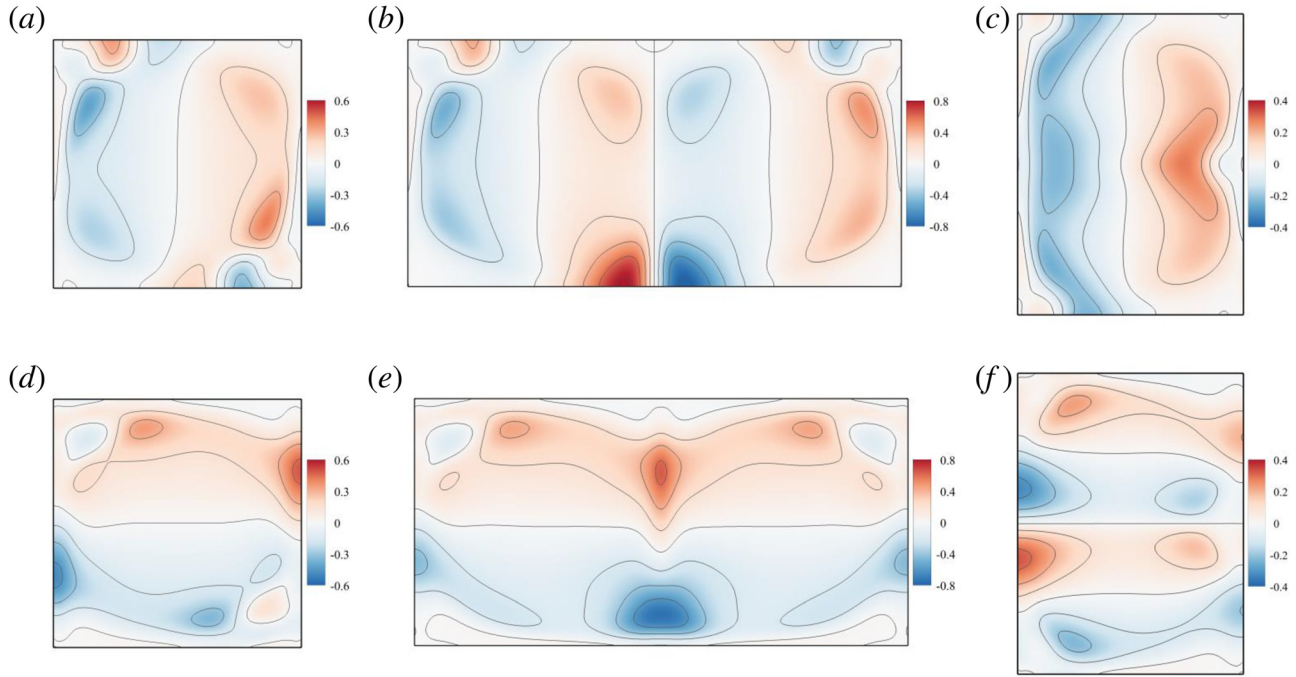
To quantitatively describe the vorticity flux as functions of the flow control parameters, we calculate the average of σ_i^* along the horizontal top and bottom walls. Because positive and negative values of σ_i^* simply imply the vorticity that enters the flow with opposite rotating direction, we take the absolute values of σ_i^* to do the average, namely, $\bar{\sigma} = (\langle|\sigma_z^*|\rangle_{top} + \langle|\sigma_z^*|\rangle_{bottom})/2$. Figure 7(a) shows the aspect ratio dependence of average vorticity flux $\bar{\sigma}$ at $10^5 \leq Ra \leq 10^6$, $Pr = 0.71$, and $0.75 \leq \Gamma \leq 6$. We can see that with the increase in Γ, the average vorticity flux along the horizontal walls and monotonously increases and gradually approach an asymptotic value. We then normalize $\bar{\sigma}$ with $\bar{\sigma}(\Gamma = 1)$, and all data fall on top of each other and the shape of $\bar{\sigma}$ do not change with Ra, as shown in Fig. 7(b). The results shown here thus suggest universal properties of vorticity flux along the heating and cooling walls with respect to different Ra.

C. Vorticity production due to buoyancy

The vorticity transport equation for incompressible thermal convection can be obtained by taking the curl of the momentum equation, which is written as[33]

$$\frac{\partial \boldsymbol{\omega}}{\partial t} + \underbrace{\mathbf{u} \cdot \nabla \boldsymbol{\omega}}_{\text{vorticity advection}} = \underbrace{\boldsymbol{\omega} \cdot \nabla \mathbf{u}}_{\text{vortex stretching/tilting}} + \underbrace{\nu \nabla^2 \boldsymbol{\omega}}_{\text{vorticity diffusion}}$$
$$+ \underbrace{\nabla \times \mathbf{F}}_{\text{body force produced vorticity}}. \tag{11}$$

In two dimensions, the velocity vector is $\mathbf{u} = (u, v, 0)$, and thus, we only have non-zero components of vorticity as $\omega_z = \partial v/\partial x - \partial u/\partial y$. There is no vortex stretching nor tilting ($\omega \cdot \nabla \mathbf{u}$ is always zero), and

FIG. 6. The [top panel, (a)–(c)] x-direction component, [bottom panel, (d)–(f)] y-direction component of pressure gradients at $Ra = 10^6$, $Pr = 0.71$, (a) and (d) $\Gamma = 1$, (b) and (e) $\Gamma = 2$, (c) and (f) $\Gamma = 0.75$.
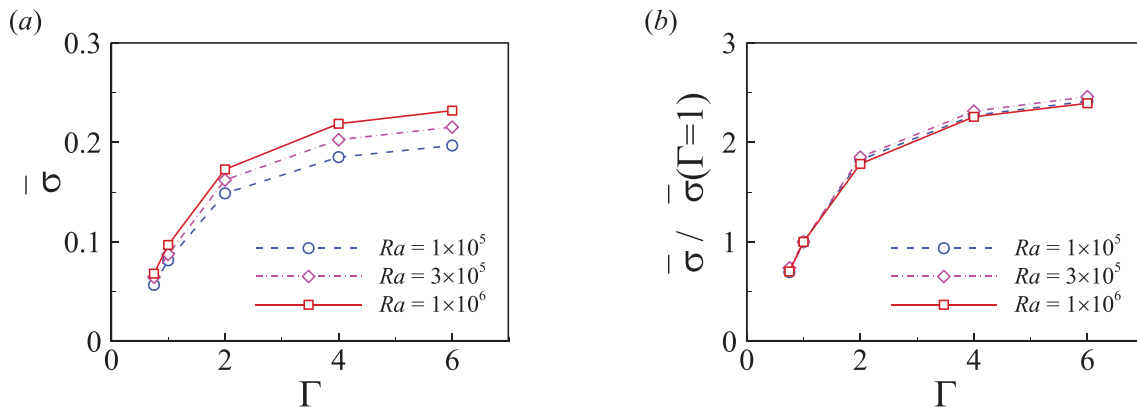
thus, vorticity production does not come from shearing effects in two dimensions. In addition, the body force (i.e., buoyancy) is $\mathbf{F} = [0, g\beta_T(T - T_0), 0]$; then, the above vorticity transport equation can be rewritten as

$$\frac{\partial \boldsymbol{\omega}_z}{\partial t} + \mathbf{u} \cdot \nabla \boldsymbol{\omega}_z = \nu \nabla^2 \boldsymbol{\omega}_z + g\beta_T \frac{\partial T}{\partial x}. \tag{12}$$

With the non-dimensional group in Eq. (2), the dimensionless vorticity transport equation for incompressible thermal flows is written as

$$\frac{\partial \omega_z^*}{\partial t^*} + \mathbf{u}^* \cdot \nabla \boldsymbol{\omega}_z = \sqrt{\frac{Pr}{Ra}} \nabla^2 \boldsymbol{\omega}_z^* + \frac{\partial T^*}{\partial x^*}. \tag{13}$$

In Fig. 8, we further provide the contour of vorticity produced by buoyancy, namely, the contour of $(\nabla \times \mathbf{F})^*$. An interesting finding is that the position of buoyancy-produced vorticity accumulates exactly where the vortices lay. Specifically, in the $\Gamma = 1$ cell [see Fig. 8(a)], counterclockwise rotated buoyancy-produced vorticity accumulates near the left-top and right-bottom corner of the cell, where counter-clockwise rotated corner vortices exist [compared to Fig. 2(a)]. In

FIG. 7. Average dimensionless vorticity flux $\sigma_i^* = -\sqrt{Pr/Ra} \cdot n_j \cdot \partial_j \cdot \omega_i^*$ along the top and bottom walls: (a) $\bar{\sigma} = (\langle|\sigma_z^*|\rangle_{top} + \langle|\sigma_z^*|\rangle_{bottom})/2$, (b) normalized $\bar{\sigma}/\bar{\sigma}(\Gamma = 1)$ at $10^5 \leq Ra \leq 10^6$, $Pr = 0.71$, and $0.75 \leq \Gamma \leq 6$.
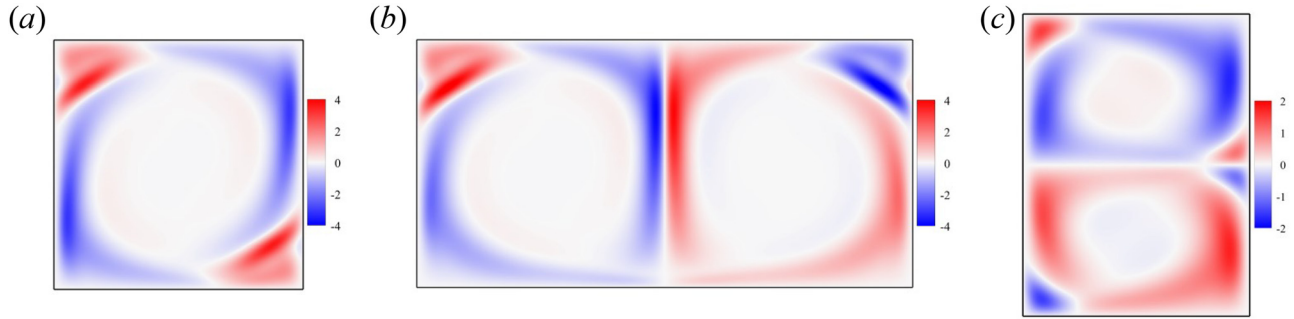
FIG. 8. Contour of vorticity produced by buoyancy, i.e., $(\nabla \times \mathbf{F})^*$, at $Ra = 10^6$, $Pr = 0.71$, and (a) $\Gamma = 1$, (b) $\Gamma = 2$, and (c) $\Gamma = 0.75$.

addition, clockwise rotated buoyancy-produced vorticity accumulates and forms the edge of the main clockwise rotating vortex. Thus, in Fig. 8, the red color region represents counterclockwise rotating vortices, and the blue color region represents the clockwise rotating vortices. We can also observe similar patterns in the $\Gamma > 1$ and the $\Gamma < 1$ cell. We propose to use the contour of buoyancy-produced vorticity, that is, $(\nabla \times \mathbf{F})^*$, as a metric to visualize the vortex in the RB convection. It should be mentioned that at present, this approach is only valid for two-dimensional flow, and extension to three-dimensional flows deserves future investigation.

We also check the amount of vorticity, without regard to direction, which is measured by enstrophy $\omega^2/2$. The enstrophy transport equation can be obtained via the inner production of $\boldsymbol{\omega}$ with Eq. (11), which is written as[33]

$$\frac{\partial\left(\frac{1}{2}\omega^2\right)}{\partial t} + \mathbf{u} \cdot \nabla\left(\frac{1}{2}\omega^2\right) = \boldsymbol{\omega} \cdot \boldsymbol{\omega} \cdot \mathbf{S} + \nu\nabla^2\left(\frac{1}{2}\omega^2\right)$$
$$- \nu(\nabla\omega)^2 + \boldsymbol{\omega} \cdot (\nabla \times \mathbf{F}). \quad (14)$$

Here, $\mathbf{S} = (\partial_j u_i + \partial_i u_j)/2$ denotes the strain rate tensor. In two dimensions, the term $\boldsymbol{\omega} \cdot \boldsymbol{\omega} \cdot \mathbf{S}$ is always zero. With the non-dimensional group in Eq. (2), the dimensionless enstrophy transport equation for incompressible thermal flows in two dimensions is written as

$$\frac{\partial\left(\frac{1}{2}\omega_z^{*2}\right)}{\partial t} + \mathbf{u}^* \cdot \nabla\left(\frac{1}{2}\omega_z^{*2}\right)$$
$$= \sqrt{\frac{Pr}{Ra}}\nabla^2\left(\frac{1}{2}\omega_z^{*2}\right) - \sqrt{\frac{Pr}{Ra}}(\nabla\omega_z^*)^2 + \omega_z^* \cdot \frac{\partial T^*}{\partial x^*}. \quad (15)$$
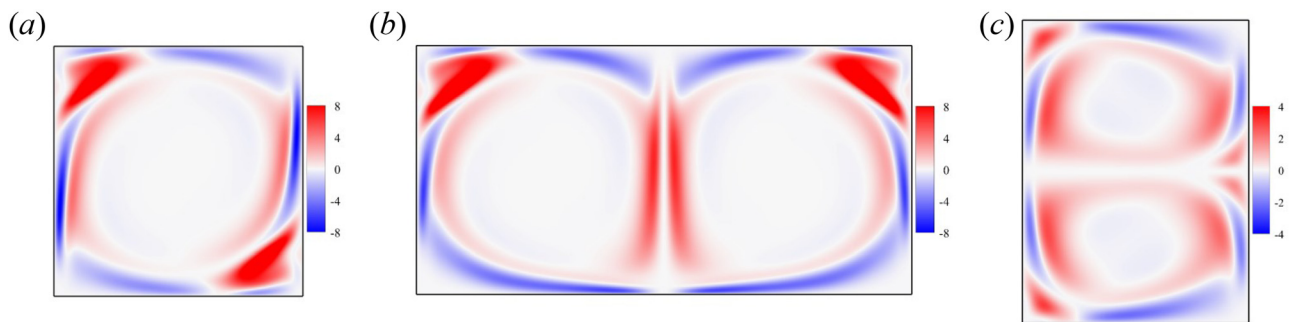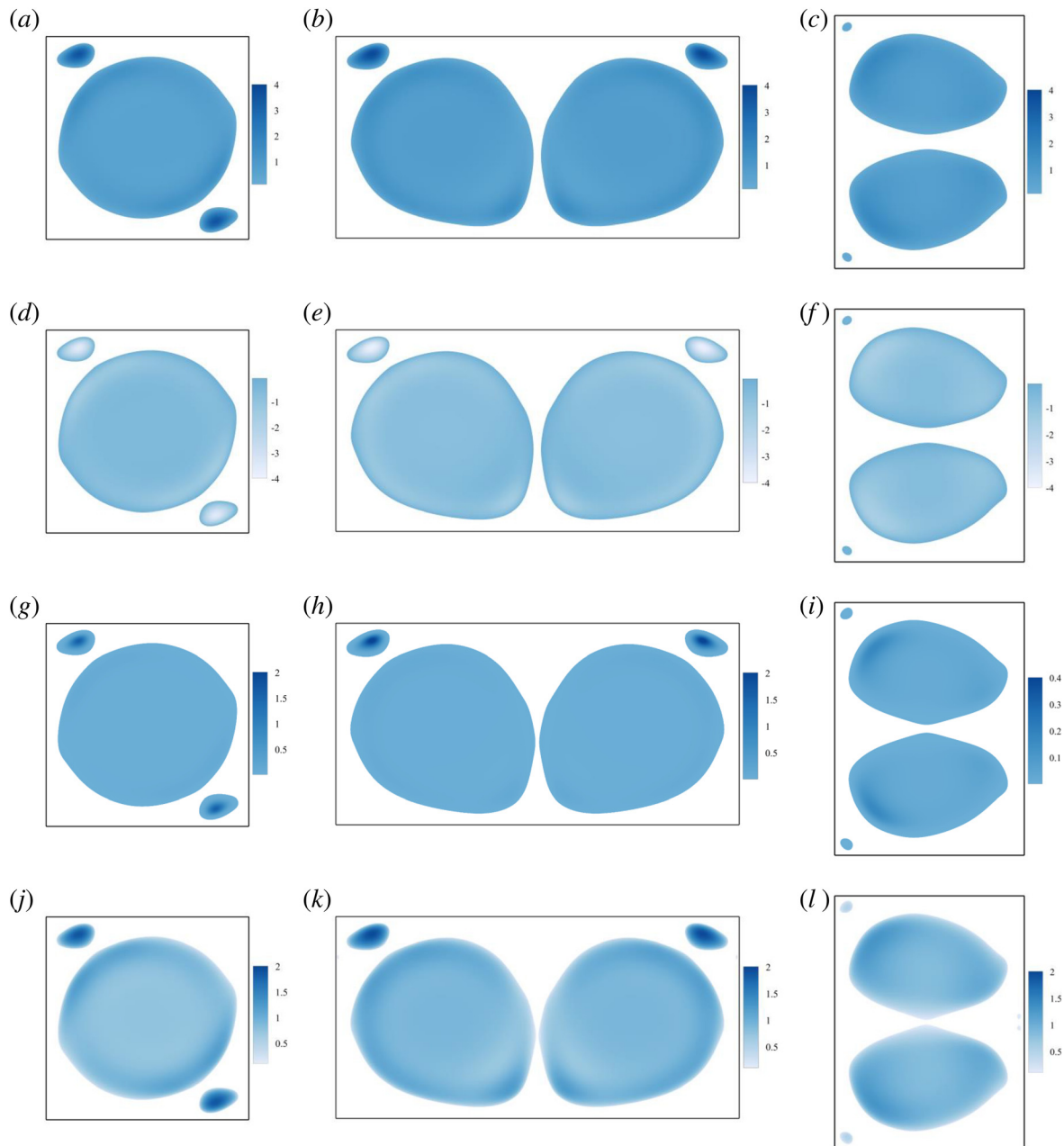
In Fig. 9, we provide the contour of enstrophy produced by buoyancy. We can see that due to buoyancy, intense enstrophy production (or destruction) occurs at the inner (or outer) edge of the main vortices; intense enstrophy production also occurs at regions of corner vortices. Analysis of spatial distribution of buoyancy-produced vorticity and buoyancy-produced enstrophy indicates that buoyancy significantly affects the flow structure in the Rayleigh–Bénard convection, and contour of buoyancy-produced vorticity and buoyancy-produced enstrophy can be used to visualize the vortices in the two-dimensional Rayleigh–Bénard convection.

It should be noted that the precise definition of a vortex is still an open question. Previously, various criteria to identify a vortex have been proposed.[34–37] In Fig. 10, we show the vortex identification using the Q-criterion,[34] the λ_2-criterion,[35] the Δ-criterion,[36] and the swirling-strength criterion[37] in the RB convection. Although those methods can be used to identify the vortices region, they failed to indicate the rotating direction of the vortices. Our method can be used to identify the vortices regions as well as the rotating direction of the vortices, which serves as an efficient vortex visualization approach. Overall, our analysis of the vorticity distribution provides an alternative understanding of the flow structure in the thermal convection cells.

D. Vorticity transport due to advection and diffusion

The vorticity redistribution mechanism is mainly due to advection and diffusion transport. In Fig. 11(a), we show the contour of the vorticity component ω_z^* in the $\Gamma = 1$ cell. We can observe strong positive values of ω_z^* (i.e., counterclockwise rotated vorticity) mainly

FIG. 9. Contour of enstrophy produced by buoyancy, that is, $[\boldsymbol{\omega} \cdot (\nabla \times \mathbf{F})]^*$, at $Ra = 10^6$, $Pr = 0.71$ and (a) $\Gamma = 1$, (b) $\Gamma = 2$, and (c) $\Gamma = 0.75$.

FIG. 10. Vortex identification using (a)–(c) the Q-criterion (contour of $Q > 0.1$), (d)–(f) the λ_2-criterion (contour of $\lambda_2 < -0.1$), (g)–(i) the Δ-criterion (contour of $\Delta > 10^{-6}$), (j)–(l) the swirling-strength criterion (contour of $\lambda_{c_i} > 0.1$) at $Ra = 10^6$, $Pr = 0.71$, and $\Gamma = 1$ (left-column), $\Gamma = 2$ (middle-column), $\Gamma = 0.75$ (right-column).

appear near the walls, and it is near zero in the bulk region of the cell. This can be simply understood as the velocity gradients are large near the wall, as evident from the clockwise rotated large-scale circulation "wind" in the cell [see Fig. 2(a)]. A fluid particle near the left bottom (or the right top) wall will first feel the influence of the large-scale circulation and gain some vorticity. After some time, it will move up (or down) along the vertical walls and diffuse out from the wall; thus, the

thickness of the diffusion layer for vorticity near the left (or the right) wall will grow from the bottom (or top) to top (or bottom). In Fig. 11(b), we further show advection of vorticity $\mathbf{u}^* \cdot \nabla \omega_z^*$ and we can see that two pairs of counter-rotating vorticity coexist along each of the four walls. Near the wall, the advection of vorticity [see Fig. 11(b)] is strongly influenced by the redistribution of wall-produced vorticity. Taking the top wall as an example, at around $0.15 < x^* < 0.3$, negative
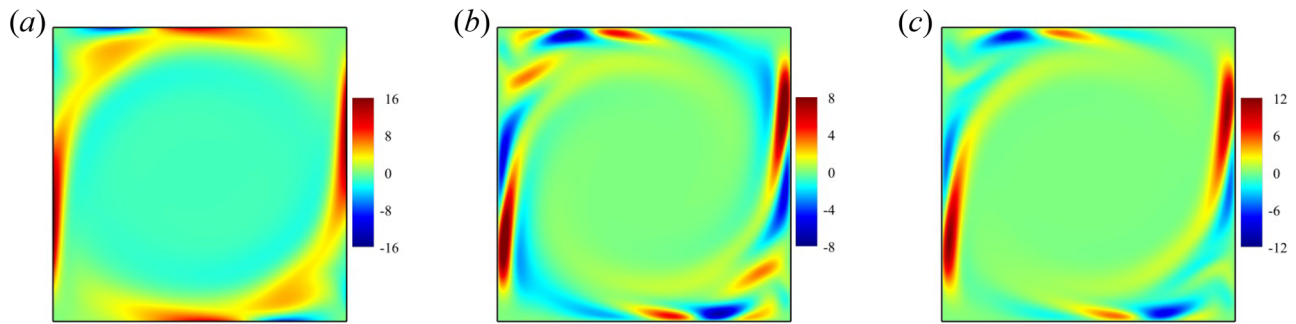
FIG. 11. Contour of (a) vorticity ω_z^*, (b) vorticity advection $\mathbf{u}^* \cdot \nabla \omega_z^*$, (c) vorticity diffusion $\sqrt{Pr/Ra}\nabla^2 \omega_z^*$ at $Ra = 10^6$, $Pr = 0.71$, and $\Gamma = 1$.

values of vorticity are entering the fluid [as evident by the valley in vorticity flux profile shown in Fig. 5(a), see more discussion in Sec. III B], which corresponds to the advection of clockwise rotated vorticity [i.e., a negative value in the contour of Fig. 11(b)]. On the contrary, at around $0.35 < x^* < 0.5$, positive values of vorticity are entering the fluid [as evident by the peak in vorticity flux profile shown in Fig. 5(a)], which corresponds to the advection of counterclockwise rotated vorticity [i.e., positive value in the contour of Fig. 11(b)]. Similarly, we can analyze the distribution of vorticity advection near the other three walls. As for the diffusion of vorticity due to the viscous effect, the pattern of vorticity diffusion is similar to that of vorticity advection [see Fig. 11(c)], and the main differences are caused by the production of either counterclockwise or clockwise rotated vorticity due to buoyancy. Meanwhile, from Fig. 11, we can see that in the $\Gamma = 1$ cell, the redistribution of vorticity advection and vorticity diffusion preserves top-bottom antisymmetric property. In the RB convection with $\Gamma = 2$ or $\Gamma = 0.75$, the aspect ratio does not significantly influence the vorticity transport. For the sake of clarity, we will not repeat the detailed discussion here, but only show the contour plot in the Appendix.

IV. CONCLUSIONS

In this work, we analyzed the vorticity production and transport in the RB convection. Specifically, with flow field and temperature field information (via solving fluid flows and heat transfer equations), we calculated each term in the vorticity transport equation. We examined the vorticity advection, diffusion, and production due to buoyancy and wall shear stress. The main findings are summarized as follows:

(1) The flow structure and temperature distribution vary with Γ greatly due to multiple vortices interaction. In addition to vorticity redistribution, buoyancy produces significant vorticity in the bulk region, resulting in a richer vortices structure.
(2) The main vortices and the corner vortices can be visualized via the contour of buoyancy-produced vorticity. This method can be used to identify the vortices regions as well as the rotating direction of the vortices, which serves as an efficient vortex visualization approach.
(3) The spatial distribution of vorticity flux along the heating and cooling walls is positively correlated with that of Nu, suggesting the amount of vorticity that enters the flow is directly related to the amount of thermal energy that enters the flow.

FIG. 12. Contour of (a) vorticity ω_z^*, (b) vorticity advection $\mathbf{u}^* \cdot \nabla \omega_z^*$, (c) vorticity diffusion $\sqrt{Pr/Ra}\nabla^2 \omega_z^*$ at $Ra = 10^6$, $Pr = 0.71$, and $\Gamma = 2$.
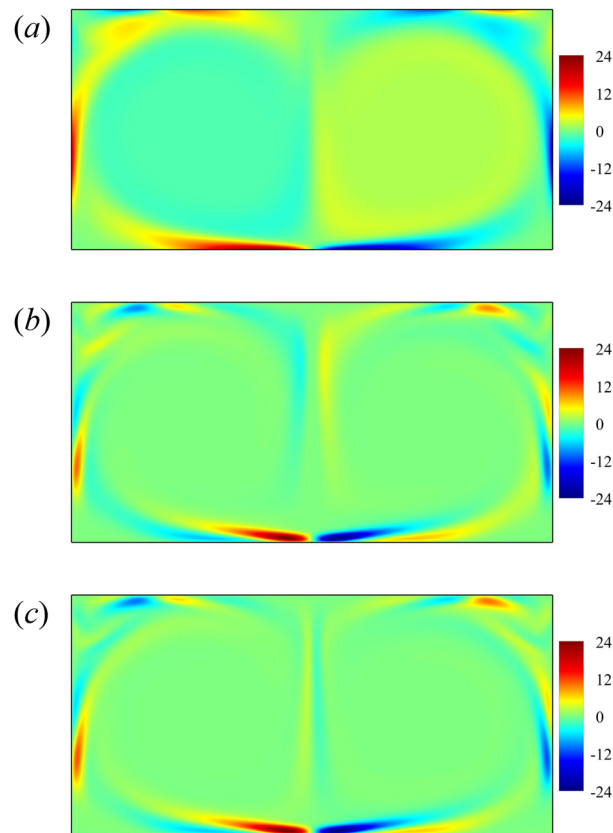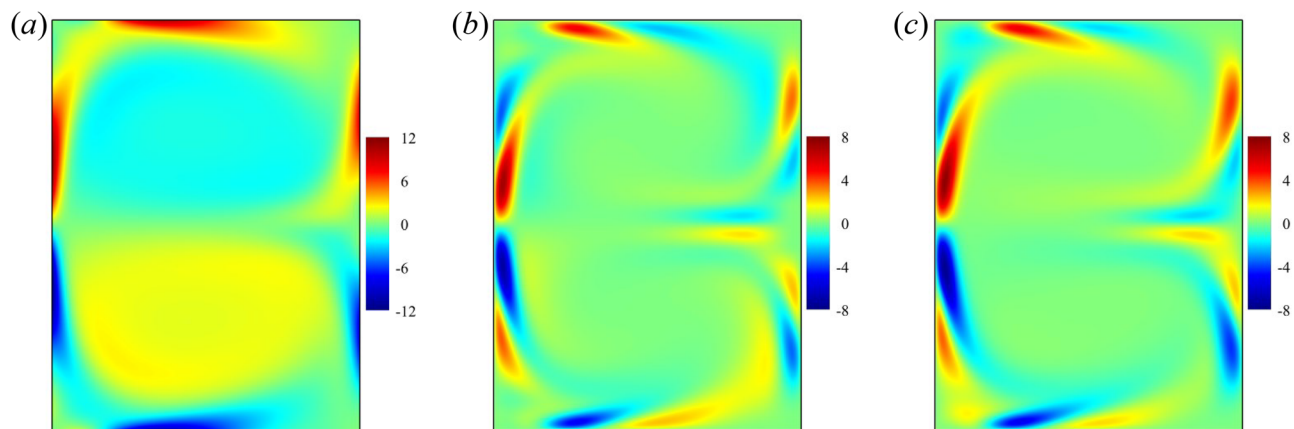
FIG. 13. Contour of (a) vorticity ω_z^*, (b) vorticity advection $\mathbf{u}^* \cdot \nabla \omega_z^*$, (c) vorticity diffusion $\sqrt{Pr/Ra}\nabla^2 \omega_z^*$ at $Ra = 10^6$, $Pr = 0.71$, and $\Gamma = 0.75$.

AUTHOR DECLARATIONS

Conflict of Interest

The authors declare no competing interests.

DATA AVAILABILITY

The data that support the findings of this study are available from the corresponding author upon reasonable request.

APPENDIX: VORTICITY TRANSPORT IN $\Gamma = 2$ CELL AND $\Gamma = 0.75$ CELL

In the RB convection with $\Gamma = 2$, the clockwise (or counterclockwise) rotated main vortex sitting in the left-half (or right-half) of the cell induce counterclockwise (or clockwise) rotated vorticity near the horizontal walls (see Fig. 12). In the RB convection with $\Gamma = 0.75$, the clockwise (or counterclockwise) rotated main vortex sitting in the top-half (or bottom-half) of the cell induce counterclockwise (or clockwise) rotated vorticity near the vertical walls (see Fig. 13). As for the differences among vorticity, vorticity advection, and vorticity diffusion, one may refer to the previous discussion in the $\Gamma = 1$ cell.

REFERENCES

[1]H. Omidvar, E. Bou-Zeid, Q. Li, J.-P. Mellado, and P. Klein, "Plume or bubble? Mixed-convection flow regimes and city-scale circulations," J. Fluid Mech. **897**, A5 (2020).

[2]R. K. Bhagat, M. D. Wykes, S. B. Dalziel, and P. Linden, "Effects of ventilation on the indoor spread of COVID-19," J. Fluid Mech. **903**, F1 (2020).

[3]A. Xu, S. Tao, L. Shi, and H.-D. Xi, "Transport and deposition of dilute microparticles in turbulent thermal convection," Phys. Fluids **32**, 083301 (2020).

[4]R. K. Shah and D. P. Sekulic, *Fundamentals of Heat Exchanger Design* (John Wiley & Sons, 2003).

[5]D. Lohse and K.-Q. Xia, "Small-scale properties of turbulent Rayleigh-Bénard convection," Annu. Rev. Fluid Mech. **42**, 335–364 (2010).

[6]K.-Q. Xia, "Current trends and future directions in turbulent thermal convection," Theor. Appl. Mech. Lett. **3**, 052001 (2013).

[7]Y.-Z. Zhang, C. Sun, Y. Bao, and Q. Zhou, "How surface roughness reduces heat transport for small roughness heights in turbulent Rayleigh–Bénard convection," J. Fluid Mech. **836**, R2 (2018).

[8]D.-L. Dong, B.-F. Wang, Y.-H. Dong, Y.-X. Huang, N. Jiang, Y.-L. Liu, Z.-M. Lu, X. Qiu, Z.-Q. Tang, and Q. Zhou, "Influence of spatial arrangements of roughness elements on turbulent Rayleigh-Bénard convection," Phys. Fluids **32**, 045114 (2020).

[9]S.-D. Huang, M. Kaczorowski, R. Ni, K.-Q. Xia *et al.*, "Confinement-induced heat-transport enhancement in turbulent thermal convection," Phys. Rev. Lett. **111**, 104501 (2013).

[10]S.-D. Huang and K.-Q. Xia, "Effects of geometric confinement in quasi-2D turbulent Rayleigh-Bénard convection," J. Fluid Mech. **794**, 639–654 (2016).

[11]B.-F. Wang, Q. Zhou, and C. Sun, "Vibration-induced boundary-layer destabilization achieves massive heat-transport enhancement," Sci. Adv. **6**, eaaz8239 (2020).

[12]J.-Z. Wu, Y.-H. Dong, B.-F. Wang, and Q. Zhou, "Phase decomposition analysis on oscillatory Rayleigh–Bénard turbulence," Phys. Fluids **33**, 045108 (2021).

[13]C. Sun, H.-D. Xi, and K.-Q. Xia, "Azimuthal symmetry, flow dynamics, and heat transport in turbulent thermal convection in a cylinder with an aspect ratio of 0.5," Phys. Rev. Lett. **95**, 074502 (2005).

[14]H.-D. Xi and K.-Q. Xia, "Flow mode transitions in turbulent thermal convection," Phys. Fluids **20**, 055104 (2008).

[15]H.-D. Xi, Y.-B. Zhang, J.-T. Hao, and K.-Q. Xia, "Higher-order flow modes in turbulent Rayleigh–Bénard convection," J. Fluid Mech. **805**, 31–51 (2016).

[16]A. Xu, X. Chen, F. Wang, and H.-D. Xi, "Correlation of internal flow structure with heat transfer efficiency in turbulent Rayleigh–Bénard convection," Phys. Fluids **32**, 105112 (2020).

[17]E. P. van der Poel, R. J. Stevens, and D. Lohse, "Connecting flow structures and heat flux in turbulent Rayleigh-Bénard convection," Phys. Rev. E **84**, 045303 (2011).

[18]E. P. van der Poel, R. J. Stevens, K. Sugiyama, and D. Lohse, "Flow states in two-dimensional Rayleigh-Bénard convection as a function of aspect-ratio and Rayleigh number," Phys. Fluids **24**, 085104 (2012).

[19]H.-Y. Zou, W.-F. Zhou, X. Chen, Y. Bao, J. Chen, and Z.-S. She, "Boundary layer structure in turbulent Rayleigh–Bénard convection in a slim box," Acta Mech. Sin. **35**, 713–728 (2019).

[20]X. Zhu and Q. Zhou, "Flow structures of turbulent Rayleigh–Bénard convection in annular cells with aspect ratio one and larger," Acta Mech. Sin. **37**, 1291–1298 (2021).

[21]R. L. Panton, *Incompressible Flow* (John Wiley & Sons, 2013).

[22]P. A. Davidson, *Turbulence: An Introduction for Scientists and Engineers* (Oxford University Press, 2015).

[23]T. Lemenand, C. Habchi, D. D. Valle, and H. Peerhossaini, "Vorticity and convective heat transfer downstream of a vortex generator," Int. J. Therm. Sci. **125**, 342–349 (2018).

[24]H. Karkaba, T. Dbouk, C. Habchi, S. Russeil, T. Lemenand, and D. Bougeard, "Multi objective optimization of vortex generators for heat transfer

enhancement using large design space exploration," Chem. Eng. Process. **154**, 107982 (2020).

[25] S. Chen and G. D. Doolen, "Lattice Boltzmann method for fluid flows," Annu. Rev. Fluid Mech. **30**, 329–364 (1998).

[26] C. K. Aidun and J. R. Clausen, "Lattice-Boltzmann method for complex flows," Annu. Rev. Fluid Mech. **42**, 439–472 (2010).

[27] A. Xu, W. Shyy, and T. Zhao, "Lattice Boltzmann modeling of transport phenomena in fuel cells and flow batteries," Acta Mech. Sin. **33**, 555–574 (2017).

[28] A. Xu, L. Shi, and T. Zhao, "Accelerated lattice Boltzmann simulation using GPU and OpenACC with data management," Int. J. Heat Mass Transfer **109**, 577–588 (2017).

[29] A. Xu, L. Shi, and H.-D. Xi, "Lattice Boltzmann simulations of three-dimensional thermal convective flows at high Rayleigh number," Int. J. Heat Mass Transfer **140**, 359–370 (2019).

[30] A. Xu, L. Shi, and H.-D. Xi, "Statistics of temperature and thermal energy dissipation rate in low-Prandtl number turbulent thermal convection," Phys. Fluids **31**, 125101 (2019).

[31] A. Xu, X. Chen, and H.-D. Xi, "Tristable flow states and reversal of the large-scale circulation in two-dimensional circular convection cells," J. Fluid Mech. **910**, A33 (2021).

[32] S. Kenjereš and K. Hanjalić, "Convective rolls and heat transfer in finite-length Rayleigh-Bénard convection: A two-dimensional numerical study," Phys. Rev. E **62**, 7987 (2000).

[33] J.-Z. Wu, H.-Y. Ma, and M.-D. Zhou, *Vorticity and Vortex Dynamics* (Springer, 2007).

[34] J. Hunt, A. Wray, and P. Moin, "Eddies, stream, and convergence zones in turbulent flows," Report No. CTR-S88 (Center for Turbulence Research Report, 1988).

[35] J. Jeong and F. Hussain, "On the identification of a vortex," J. Fluid Mech. **285**, 69–94 (1995).

[36] M. S. Chong, A. E. Perry, and B. J. Cantwell, "A general classification of three-dimensional flow fields," Phys. Fluids A **2**, 765–777 (1990).

[37] J. Zhou, R. J. Adrian, S. Balachandar, and T. Kendall, "Mechanisms for generating coherent packets of hairpin vortices in channel flow," J. Fluid Mech. **387**, 353–396 (1999).